Editors' Suggestion Featured in Physics

Characteristic E-Region Plasma Signature of Magnetospheric Wave-Particle Interactions

Magnus F. Ivarsen[*]
Department of Physics, University of Oslo, Oslo 0316, Norway

Yukinaga Miyashita[†]
Space Science Division, Korea Astronomy and Space Science Institute, Daejeon 34055, South Korea

Jean-Pierre St-Maurice,[‡] Glenn C. Hussey, Brian Pitzel, Draven Galeschuk, and Saif Marei
Department of Physics and Engineering Physics, University of Saskatchewan, Saskatoon, Saskatchewan S7N 5E2, Canada

Richard B. Horne
British Antarctic Survey, Cambridge CB3 0ET, United Kingdom

Yoshiya Kasahara and Shoya Matsuda
Graduate School of Natural Science and Technology, Kanazawa University, Kanazawa 920-1192, Japan

Satoshi Kasahara and Kunihiro Keika
Department of Earth and Planetary Science, University of Tokyo, Tokyo 113-8654, Japan

Yoshizumi Miyoshi, Kazuhiro Yamamoto, and Atsuki Shinbori
Institute for Space-Earth Environmental Research, Nagoya University, Nagoya 464-8601, Japan

Devin R. Huyghebaert[§]
Department of Physics and Technology, University of Tromsø, Tromsø 9037, Norway

Ayako Matsuoka
Data Analysis Center for Geomagnetism and Space Magnetism, Kyoto University, Kyoto 606-8501, Japan

Shoichiro Yokota
Department of Earth and Space Science, Osaka University, Toyonaka 560-0043, Japan

Fuminori Tsuchiya
Planetary Plasma and Atmospheric Research Center, Tohoku University, Tohoku 980-8577, Japan

(Received 18 July 2024; revised 8 January 2025; accepted 27 February 2025; published 11 April 2025)

Plasma waves in the magnetosphere scatter electrons, causing them to precipitate into Earth's atmosphere, imparting their temporal characteristics to diffuse auroras. In a case study of conjugate radar and satellite observations, we demonstrate a close and unprecedented association between enhanced electrostatic cyclotron harmonic wave activity in the magnetosphere and the appearance of meter-scale plasma turbulence a few seconds later in the lower ionosphere on nearby magnetic field lines. Such direct structuring of the ionosphere carries implications for our understanding of space weather.

DOI: 10.1103/PhysRevLett.134.145201

[*]Present address: Department of Physics and Engineering Physics, University of Saskatchewan, Saskatoon, Saskatchewan, Canada.
[†]Also at Department of Astronomy and Space Science, Korea University of Science and Technology, Daejeon 34113, South Korea.
[‡]Also at Department of Physics and Astronomy, University of Western Ontario, London, N6A 3K7 Ontario, Canada.
[§]Also at Department of Physics and Engineering Physics, University of Saskatchewan, Saskatoon, Saskatchewan, Canada.

Introduction—During major disturbances in geospace much energy is imparted from the solar wind to Earth's atmosphere. Large-scale electrical currents and the creation of strong electric fields at ionospheric altitudes ensues [1,2]. The effect is widespread plasma turbulence [3,4].

The Farley-Buneman (FB) instability features prominently in the ionosphere's lower layers, the E region [5,6]. The intense meter-scale FB structures are excited when the relative drift (polarization electric field) between the strongly magnetized electrons and largely unmagnetized ions exceeds the local ion-acoustic speed [7]. The requirement for a large relative drift means that the structures are found in Hall currents regions, the auroral electrojets. Radio signals that scatter off these waves have been coined the "radar aurora" [8].

The ionosphere largely draws energy from diffuse auroras at night [9,10], produced when hot electrons near the ring current interact with naturally occurring waves through cyclotron resonance, causing pitch angle scattering and subsequent precipitation into the atmosphere [11–13]. Mechanisms notably include whistler-mode chorus and electrostatic cyclotron harmonic (ECH) waves [11,14–17].

Recent advances have demonstrated that temporal oscillations in chorus wave activity are closely linked to the dynamic behavior of pulsating auroras [18–20]. This important discovery documents that the signature of "magnetospheric" processes can be reproduced in "ionospheric" processes.

The physical route for such processes to impact the ionosphere is twofold. First, the precipitating particles quasi-instantaneously introduce a perpendicular electric field. Second, local ionization of the plasma will modulate conductivities through chemistry with its fast increase in ion production rates courtesy of impacting particles recombining with the surrounding plasma, albeit somewhat more slowly [21].

Conjugate radar observations have established a firm link between auroral pulsations and electrodynamic oscillations in the ionosphere. Notably, periodic modulations in the plasma density, conductivity, and electric field strength are associated with pulsating auroras [22,23]. *In situ* observations have revealed the presence of downward field-aligned (likely thermal) currents on the edges of such patches [24], and the filamentation (field-tube structuring) of those currents have been found to match the spatial signature of E-region plasma turbulence [25,26].

Motivated by the above, we hypothesize that turbulent structuring of the electric and density fields in the auroral E region can be, at their core, *directly* caused by the wave-particle interactions in the diffuse aurora, with the aurora as a mediator of the driving signal. In testing this hypothesis for a case study, FB turbulence takes center stage. Individual FB waves in the radar aurora are so intense and short-lived that they quickly dissipate and are replaced by new waves [27–29]. When and where FB waves grow will thus depend on the spatiotemporal location of their sources.

Data—To investigate whether magnetospheric wave activity can act as a direct driver of small-scale plasma turbulence in the ionosphere, we searched for space-ground conjunctions that took place when the Japanese inner-magnetosphere spacecraft *Arase* was close to magnetic equator, with a Northern Hemisphere footprint that was within the field of view of the new Canadian ionospheric continuous-wave E-region bistatic experimental auroral radar (ICEBEAR) and in the presence of active auroras. Combing through coincident data collected between January 2020 and June 2023, we found one such event.

Figure 1(a) shows an annotated optical image of diffuse, pulsating auroras, taken with the Transition Region Explorer (TREx) RGB system at Rabbit Lake [30]. The system was switched on at dusk, around midway into the event. Superposed on Fig. 1(a) is the point-cloud distribution of a few thousand radar echoes that were detected in a 3-s interval following 06:56:45 universal time (UT) on May 12, 2021. The radar echoes were measured by ICEBEAR, a coherent scatter radar that combines multiple interferometry links with a coded pseudo-random continuous-wave signal to achieve high resolution 3D radar data [31,32].

In Fig. 1(a), and in Videos S1 and S2 in the Supplemental Material [35], the radar echoes cluster between evolving pulsating auroral patches along their poleward flank. Electric field enhancements maximize *outside* the patches [23], as opposed to the patches' interiors, where elevated conductivities may short out the field entirely [24,41]. Each received echo indicates the presence of turbulent electrojet currents in the space around the pulsating patches.

The direct cause of these turbulent currents were observed by *Arase* in the distant equatorial magnetosphere. *Arase*'s orbit during the event is shown in Figs. 1(c) and 1(d). The orbit has an apogee of 32 000 km and a perigee of 400 km, an inclination angle of 31°, and a period of 570 min [42]. Figure 1(e) substantiates the relative accuracy of the TS04 model [43] in mapping *Arase*'s magnetic footprint from its orbit down to the Northern Hemisphere E region, a mapping that is, in general, made uncertain by the ubiquitous presence of Alfvén waves and field-aligned currents [44]. *Arase*'s footprint is estimated to lie on the equatorward flank of the pulsating auroras, whose poleward flank is occupied by radar echoes.

The magnetospheric measurements used in the present Letter are summarized in Fig. 2. We analyze mostly electric field power spectra on frequencies between 0.1 and 20 kHz, a range in which whistler-mode chorus waves and electrostatic cyclotron harmonic waves often appear. The measurements originate in the plasma wave experiment (PWE) instrument onboard *Arase*. The data product consists of electric field power spectrograms [45,46], shown in Fig. 2(a). In addition to wave power, we also collected data from *Arase*'s onboard medium-energy particle

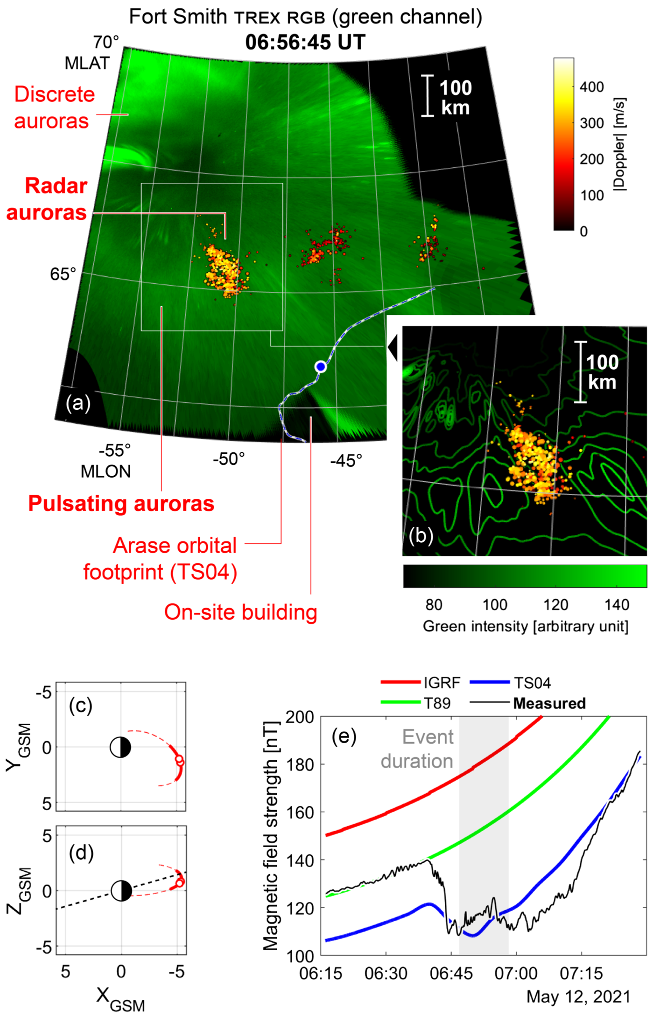

FIG. 1. A conjunction on May 12, 2021 between the ICEBEAR radar, a TREx auroral camera, and the ionospheric footprint of *Arase*. (a),(b) A 3-s auroral image (the green channel of the RGB triplet) projected onto the ionosphere following Ref. [33], with the locations of radar echoes (color coded according to Doppler shift), all shown in geomagnetic coordinates (altitude-adjusted corrected geomagnetic coordinates [34]). The ionospheric footprint of the magnetospheric spacecraft *Arase* is shown as a blue circle. (b) Enlargement of a radar aurora shape that appears lodged between two pulsating patches (see also Video S2 [35]). (c),(d) *Arase*'s journey in the magnetosphere in geocentric solar magnetospheric (GSM) coordinates, with magnetic equator appearing as a dashed black line. (e) Compares the modeled (red, green, and blue) with the measured (black) magnetic field strength along *Arase*'s trajectory. See Fig. 5 in the Appendix A for a graphical representation. IGRF, International Geomagnetic Reference Field.

detector, which detects 7–87 keV precipitating electrons [47], shown in Fig. 2(b). Finally, Fig. 2(c) shows the auroral electrojet index (SME index, black line, left axis) and the SymH-index (red line, right axis).

Geospace description: We are now in a position to formulate and interpret the conditions of geospace during

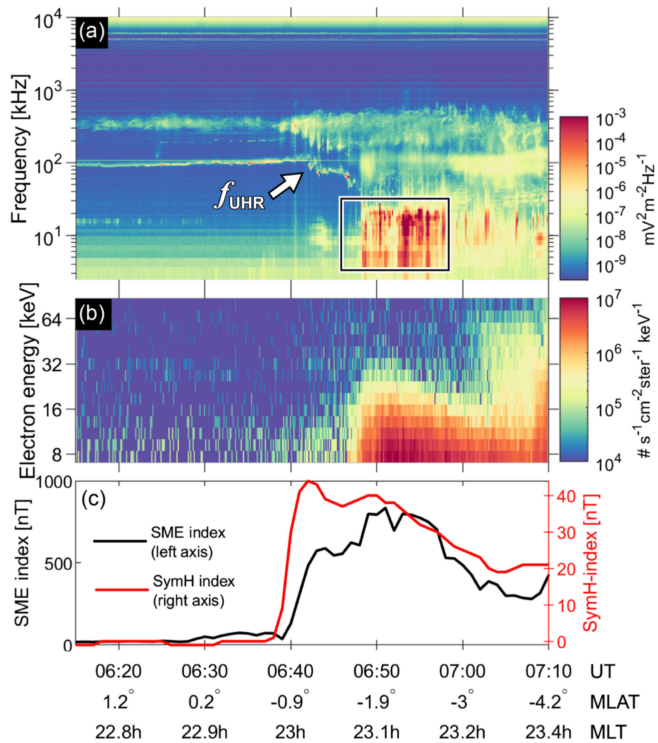

FIG. 2. (a) High-frequency electric field spectrogram from *Arase*'s PWE instrument. The black rectangle refers to the analysis in Fig. 3. (b) Precipitating electron energy flux from *Arase*'s medium-energy particle detector (data from the low-energy detector was unavailable). The data show pitch angles lower than 10°, but we additionally confirmed that it was consistent with the parallel-flux data (pitch angles $< 2°$). (c) The SuperMAG Electrojet (SME) index (left axis) and the Symmetric H (SymH) index (right axis). The three x axes show time in UT (on 12 May 2021) and *Arase*'s orbital location in the magnetosphere.

our event. The conjunction, which was preceded by a geomagnetically quiet period, took place during drastic and coincident increases in the SME and SymH indices [Fig. 2(c)]. The strong impulse in these indices was the effect of a sudden ninefold jump in the solar wind dynamic pressure (not shown), which led to magnetospheric compression [48].

Around 06:40 UT, *Arase*, situated at the equator [$-1°$ magnetic latitude (MLAT)], suddenly found itself outside the plasmasphere, witnessed by the rapid decrease in the upper hybrid resonance frequency [f_{UHR} in Fig. 2(a) [49]]. *Arase* was thus experiencing optimal conditions for the observation of ECH waves [50,51], waves that were simultaneously given access to hot ring current electrons [52]. The loss of these electrons into Earth's atmosphere resulted in the diffuse auroras observed with the TREx RGB system in Figs. 1(a) and 1(b) and in Video S2 [35].

Penetrating electric fields: Next, we shall compare the wave power measured by *Arase* with the FB turbulence echo "detection rates" measured by the ICEBEAR radar, the rate at which ICEBEAR's range and Doppler gates are receiving signals. That metric is exceedingly simple: it entails counting the raw number of radar echoes detected for each time step (1 s). With the premise of extant FB waves being ephemeral, changes in this metric will reflect changes in the turbulent driver within ICEBEAR's field of view.

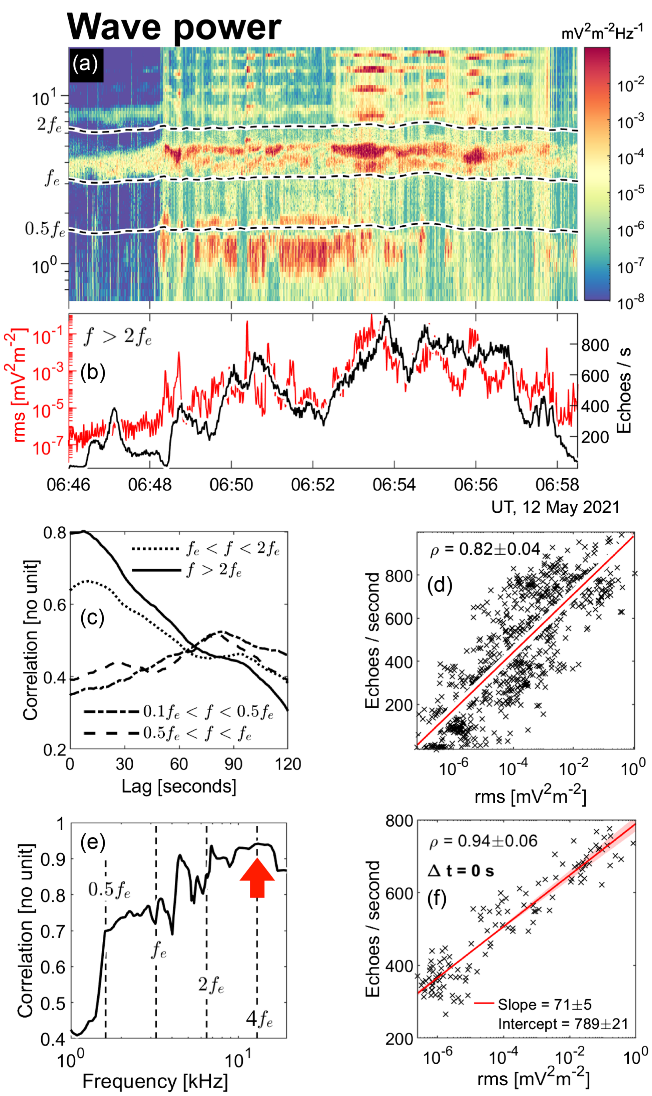

FIG. 3. (a) Electric field spectrogram observed between 06:46:00 and 06:58:30 UT on May 12, 2021, with three frequencies indicated ($0.5f_e$, f_e, and $2f_e$). (b) rms for the $2f_e < f < 19.45$ kHz frequency range, with the ICEBEAR echo detection rate superposed (right axes). (c) Cross-correlation analysis between the echo rates and the rms for all four frequency ranges. (d) Scatter plot of the data in (b), with the ECH wave power having been shifted 7 s back in time; Pearson correlation coefficient for a log-linear fit, with an error margin given by 95% (3σ) confidence intervals is indicated. (e) The highest cross-correlation obtained from a moving window in frequency (7 logarithmic increments out of 132) and time (2 min), with a maximum allowed lag of 9 s. (f) Scatter plot akin to (d), but for frequencies around $4f_e$ ($11.5 < f < 15$ kHz), during a 2-min window centered on 06:52:32 UT (at zero lag).

Figure 3(a) shows wave power at 1-s cadence [53], encompassing the interval 06:46:00–06:58:30 UT and highlighting three frequencies with dashed black lines ($0.5f_e$, f_e, and $2f_e$, with f_e being the local electron cyclotron frequency, calculated using the dc magnetic field data from the magnetic field experiment [54]). Figure 3(b) uses a solid red line to show the integrated power (referred to as rms, or root-mean-square) in the $f > 2f_e$ range, and we now superpose the ICEBEAR echo detection rate with a solid black line (right axis). Figure 3(c) shows the result of a cross-correlation analysis performed between the echo detection rates and the wave power rms in four frequency ranges. For the $f > 2f_e$ range, we observe strong correlation [Pearson coefficient $\rho = 0.82$, shown in Fig. 3(d)], with a peak lag of 7 s, indicating that optimal correlation is obtained by shifting the *Arase* observations 7 s back in time. This lag should be compared to the time of flight for the electrons of around 1 s [55,56], and we note that the correlation is similar for a 1-s lag. Figure 3(e) shows explicitly how this result depends on frequency. It shows a cross-correlation analysis on a moving window both in time and frequency. There is a noticeable uptick in correlation at $f = 2f_e$, and at $f = 4f_e$ the correlation coefficient reaches

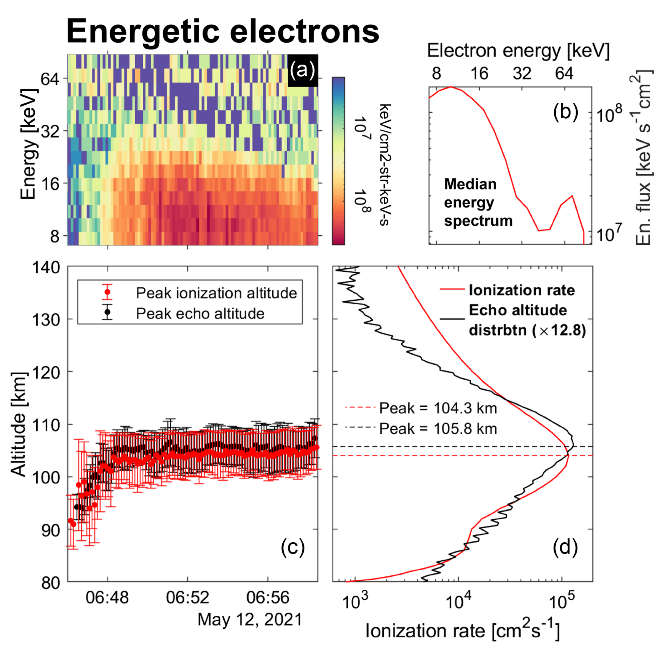

FIG. 4. (a) Precipitating particle energy flux measured by *Arase*. (b) Median energy spectrum. (c) ICEBEAR echo altitudes as a function of time (black dots) and the peak emission altitude based on the electron energy flux (red error bars), using generalized parametrization of numerical models [57], including the mass spectrometer incoherent scatter model of Earth's atmosphere [58]. (d) Overall ICEBEAR echo altitude distribution ("distrbtn"; black) and auroral emission altitude profile (red), peak altitudes indicated.

0.94. We note that this latter correlation was determined at a zero lag (< 1 s), on the order of the time of flight of the electrons themselves. The p values (probabilities that the correlations were spurious) obtained for the two quoted coefficients were zero at floating point precision.

Ionization in the lower ionosphere: Having demonstrated a close correspondence between the evolution of ECH wave power and that of turbulence echo detection rate, we shall next demonstrate a link between the evolution of the particle flux at *Arase*'s orbit and that of the echo detection altitudes. Figure 4(a) plots the 8–87 keV-electron energy flux. We then assume the flux is a proxy for the real precipitating energy flux, treating it to be caused by 16 monoenergetic beams of electrons (one for each energy channel). We apply parametrizations to estimate the ionization altitude profile for each beam of electrons. The cumulative profile then corresponds to the emission altitude profile of the observed auroras.

The results of this altitude analysis are shown in Figs. 4(c) and 4(d), where we likewise plot the total altitude distribution of the radar echo point cloud. The two time series in Fig. 4(c) exhibit a Pearson correlation coefficient of 0.87, and the two profiles in Fig. 4(d) match surprisingly well, with peaks in the distributions being separated by only 1.5 km. The unambiguous similarity points to a causal link between the particle-induced ionization and the distribution of radar echoes in the E region.

Discussion—At the event's onset, *Arase* had just exited the plasmasphere at the equator (orbiting from $-1.5°$ to $-3°$ MLAT) where it observed intense ($0.1\ \mathrm{mV^{-2}\,m^{-1}}$) ECH waves inside the region where such waves are confined [50,51] and capable of accelerating keV electrons toward Earth's atmosphere [14,17,50,59].

Arase's footprint in the ionosphere was likely 100–200 km south of the echo region, with diffuse auroral shapes appearing in between. The precipitating electrons inside the patches briefly accumulated at an altitude of around 104 km. There, they produced strong electric fields [60,61] and plasma density gradients by merit of ionizing the gas. The plasma can then become gradient-drift unstable [62], and at the same time, the Farley-Buneman instability may saturate [63]. Once saturated, the instability produces secondary waves [64,65] and dissipates the wave power through heating [66,67]. The high-amplitude FB waves dissipate fast, giving the turbulence the impression of being ephemeral, or instantaneous [29]. Ultimately, this allows the ensemble radio echoes from those waves to accurately reflect the changes in the instability driver on timescales larger than a second, facilitating the strong correlations between the various time series in Figs. 3(d)–3(f) and 4(c).

The resulting image is one of a self-similar and turbulent state, simultaneously measured at points in space separated by 5 Earth radii. It implies that the entire turbulent process retains a distinct "stochastic shape" that is conserved down to meter scale.

There is a causal and largely instantaneous path from the modulation of ECH waves to small-scale turbulence. It involves particle precipitation, which creates beams of electrons that modulate conductivity (ionization) and electric fields [68]. Those modulations can produce gradient-drift unstable structures [62], whose imminent decay into smaller and smaller pieces, the turbulent cascade, systematically breaks apart structures smaller in size than around 1–10 km [69,70]. The shapes, or rather, their stochastic features, are subsequently repeated in a self-similar pattern down to meter scale in magnification, at which point the initial perturbations can seed the Farley-Buneman instability and saturate its growth rates (see Fig. 5 in the Appendix A for a graphical depiction. For a statistical analysis of the data, see Appendix B).

Other driving mechanisms are readily available, such as Alfvén waves and other field-parallel acceleration mechanisms, as well as magnetospheric ion cyclotron waves, and other wave-particle interactions. However, as shown by Figs. 3(d)–3(f), the ensemble of radar echoes recreates temporal changes in the magnetospheric wave-particle interactions with remarkable fidelity; the observed evolution of small-scale plasma turbulence identifies its maker, faithfully mimicking a driving signal. In other words, the spatiotemporal evolution of the interconnected system is contained in the small-scale dissipation of turbulent energy in the dense ionosphere, information that is mediated by mode coupling.

Refreshingly and for a brief moment, then, the local space weather had a clear physical driver. The turbulent transformation of this driving signal can inform development of models that aim to predict the occurrence of plasma turbulence around auroras.

Summary—In this Letter, we have reported a conjunction between *Arase*'s Northern Hemisphere footprint and the ICEBEAR radar's field of view. *Arase* observed strong electrostatic cyclotron harmonic wave activity at the magnetic equator. On a nearby magnetic field line, ICEBEAR recorded a matching radar signal from turbulent electrojets in the space between pulsating auroras.

Our interpretation of the findings, and the only viable explanation we can find for their cause, is that an ensemble of wave-particle interactions imparted their temporal and spatial characteristics to a spatiotemporal pattern of electron precipitation. The electrons inside these structures produced pulsating auroras and introduced an associated pattern of ionization and electric field enhancements in the E region that were insensibly picked up by the growth of FB waves. The growth, saturation, and subsequent detection of these waves faithfully reflected the evolution of the underlying driver.

We conclude that the detection of small-scale plasma turbulence in the auroral E region can be applied as a diagnostic tool to quantify the whole energy input behind space weather events, a remarkable victory for the concept of mode coupling in plasma physics.

Acknowledgments—M. F. I. is thankful to F. Lind, Y. Jin, W. Miloch, and L. Clausen for stimulating discussions. This work is supported in part by the European Space Agency's Living Planet Grant No. 1000012348 and by the Research Council of Norway (RCN) Grant No. 324859. We acknowledge the support of the Canadian Space Agency (CSA) (20SUGOICEB), the Canada Foundation for Innovation (CFI) John R. Evans Leaders Fund (32117), the Natural Science and Engineering Research Council (NSERC), the Discovery grants program (RGPIN-2019-19135), the Digital Research Alliance of Canada (RRG-4802), and basic research funding from Korea Astronomy and Space Science Institute (KASI2024185002). Science data of the ERG (*Arase*) satellite were obtained from the ERG Science Center operated by ISAS/JAXA and ISEE/Nagoya University [71].

Data availability—The data of the ERG satellite includes Lv.3 MEP-e [72], Lv.2 PWE/OFA [73], Lv.2 PWE/HFA [74], and Lv.2 MGF [75]. ICEBEAR 3D echo data for 2020 and 2021 are available at [76]. SuperMAG data can be accessed at [77]. The SymH-index from NASA's OMNI service can be accessed at [78] and TREx optical data can be accessed at [79].

[1] T. Iijima and T. A. Potemra, Large-scale characteristics of field-aligned currents associated with substorms, J. Geophys. Res. **83**, 599 (1978).

[2] A. Keiling, S. Thaller, J. Wygant, and J. Dombeck, Assessing the global Alfvén wave power flow into and out of the auroral acceleration region during geomagnetic storms, Sci. Adv. **5**, eaav8411 (2019).

[3] J. D. Huba, A. B. Hassam, I. B. Schwartz, and M. J. Keskinen, Ionospheric turbulence: Interchange instabilities and chaotic fluid behavior, Geophys. Res. Lett. **12**, 65 (1985).

[4] M. Wiltberger, V. Merkin, B. Zhang, F. Toffoletto, M. Oppenheim, W. Wang, J. G. Lyon, J. Liu, Y. Dimant, M. I. Sitnov, and G. K. Stephens, Effects of electrojet turbulence on a magnetosphere-ionosphere simulation of a geomagnetic storm, J. Geophys. Res. **122**, 5008 (2017).

[5] D. T. Farley, A plasma instability resulting in field-aligned irregularities in the ionosphere, J. Geophys. Res. (1896–1977) **68**, 6083 (1963).

[6] O. Buneman, Excitation of field aligned sound waves by electron streams, Phys. Rev. Lett. **10**, 285 (1963).

[7] M. M. Oppenheim and Y. S. Dimant, Kinetic simulations of 3-D Farley-Buneman turbulence and anomalous electron heating, J. Geophys. Res. **118**, 1306 (2013).

[8] D. L. Hysell, The radar aurora, in *Auroral Dynamics and Space Weather* (American Geophysical Union (AGU), 2015), Chap. 14, pp. 191–209, 10.1002/9781118978719.ch14.

[9] P. T. Newell, T. Sotirelis, and S. Wing, Seasonal variations in diffuse, monoenergetic, and broadband aurora, J. Geophys. Res. **115**, A03216 (2010).

[10] R. M. Robinson, R. R. Vondrak, K. Miller, T. Dabbs, and D. Hardy, On calculating ionospheric conductances from the flux and energy of precipitating electrons, J. Geophys. Res. **92**, 2565 (1987).

[11] B. Ni, R. M. Thorne, Y. Y. Shprits, and J. Bortnik, Resonant scattering of plasma sheet electrons by whistler-mode chorus: Contribution to diffuse auroral precipitation, Geophys. Res. Lett. **35** (2008).

[12] J. Birn, A. V. Artemyev, D. N. Baker, M. Echim, M. Hoshino, and L. M. Zelenyi, Particle acceleration in the magnetotail and aurora, Space Sci. Rev. **173**, 49 (2012).

[13] B. Ni, J. Bortnik, Y. Nishimura, R. M. Thorne, W. Li, V. Angelopoulos, Y. Ebihara, and A. T. Weatherwax, Chorus wave scattering responsible for the Earth's dayside diffuse auroral precipitation: A detailed case study, J. Geophys. Res. **119**, 897 (2014).

[14] R. B. Horne, R. M. Thorne, N. P. Meredith, and R. R. Anderson, Diffuse auroral electron scattering by electron cyclotron harmonic and whistler mode waves during an isolated substorm, J. Geophys. Res. **108**, 14-1 (2003).

[15] J. Liang, V. Uritsky, E. Donovan, B. Ni, E. Spanswick, T. Trondsen, J. Bonnell, A. Roux, U. Auster, and D. Larson, THEMIS observations of electron cyclotron harmonic emissions, ULF waves, and pulsating auroras, J. Geophys. Res. **115**, A10235 (2010).

[16] B. Ni, J. Liang, R. M. Thorne, V. Angelopoulos, R. B. Horne, M. Kubyshkina, E. Spanswick, E. F. Donovan, and D. Lummerzheim, Efficient diffuse auroral electron scattering by electrostatic electron cyclotron harmonic waves in the outer magnetosphere: A detailed case study, J. Geophys. Res. **117**, A01218 (2012).

[17] S. Kurita, Y. Miyoshi, C. M. Cully, V. Angelopoulos, O. L. Contel, M. Hikishima, and H. Misawa, Observational evidence of electron pitch angle scattering driven by ECH waves, Geophys. Res. Lett. **41**, 8076 (2014).

[18] S. Kasahara, Y. Miyoshi, S. Yokota, T. Mitani, Y. Kasahara, S. Matsuda, A. Kumamoto, A. Matsuoka, Y. Kazama, H. U. Frey, V. Angelopoulos, S. Kurita, K. Keika, K. Seki, and I. Shinohara, Pulsating aurora from electron scattering by chorus waves, Nature (London) **554**, 337 (2018).

[19] K. Hosokawa, Y. Miyoshi, M. Ozaki, S.-I. Oyama, Y. Ogawa, S. Kurita, Y. Kasahara, Y. Kasaba, S. Yagitani, S. Matsuda, F. Tsuchiya, A. Kumamoto, R. Kataoka, K. Shiokawa, T. Raita, E. Turunen, T. Takashima, I. Shinohara, and R. Fujii, Multiple time-scale beats in aurora: Precise orchestration via magnetospheric chorus waves, Sci. Rep. **10**, 3380 (2020).

[20] Y. Miyoshi *et al.*, Penetration of MeV electrons into the mesosphere accompanying pulsating aurorae, Sci. Rep. **11**, 13724 (2021).

[21] R. W. Schunk and J. J. Sojka, A theoretical study of the lifetime and transport of large ionospheric density structures, J. Geophys. Res. **92**, 12343 (1987).

[22] K. Hosokawa, Y. Ogawa, A. Kadokura, H. Miyaoka, and N. Sato, Modulation of ionospheric conductance and electric field associated with pulsating aurora, J. Geophys. Res. **115**, A03201 (2010).

[23] K. Hosokawa, T. Motoba, A. S. Yukimatu, S. E. Milan, M. Lester, A. Kadokura, N. Sato, and G. Bjornsson, Plasma irregularities adjacent to auroral patches in the postmidnight sector, J. Geophys. Res. **115**, A09303 (2010).

[24] D. M. Gillies, D. Knudsen, E. Spanswick, E. Donovan, J. Burchill, and M. Patrick, Swarm observations of field-aligned currents associated with pulsating auroral patches, J. Geophys. Res. **120**, 9484 (2015).
[25] M. F. Ivarsen, A. Lozinsky, J.-P. St-Maurice, A. Spicher, D. Huyghebaert, G. C. Hussey, D. Galeschuk, B. Pitzel, and J. Vierinen, The distribution of small-scale irregularities in the E-region, and its tendency to match the spectrum of field-aligned current structures in the F-region, J. Geophys. Res. **128**, e2022JA031233 (2023).
[26] M. F. Ivarsen, M. D. Gillies, D. R. Huyghebaert, J.-P. St-Maurice, A. Lozinsky, D. Galeschuk, E. Donovan, and G. C. Hussey, Turbulence embedded into the ionosphere by electromagnetic waves, J. Geophys. Res. **129**, e2023JA032310 (2024).
[27] P. Prikryl, D. André, G. J. Sofko, and J. A. Koehler, Doppler radar observations of harmonics of electrostatic ion cyclotron waves in the auroral ionosphere, J. Geophys. Res. **93**, 7409 (1988).
[28] P. Prikryl, D. Andre, J. A. Koehler, G. J. Sofko, and M. J. McKibben, Evidence of highly localized auroral scatterers from 50-MHz CW radar interferometry, Planet. Space Sci. **38**, 933 (1990).
[29] M. F. Ivarsen, J.-P. St-Maurice, D. R. Huyghebaert, M. D. Gillies, F. Lind, B. Pitzel, and G. C. Hussey, Deriving the ionospheric electric field from the bulk motion of radar aurora in the E-region, J. Geophys. Res. **129**, e2024JA033060 (2024).
[30] D. M. Gillies, E. Donovan, D. Hampton, J. Liang, M. Connors, Y. Nishimura, B. Gallardo-Lacourt, and E. Spanswick, First observations from the TREx spectrograph: The optical spectrum of STEVE and the picket fence phenomena, Geophys. Res. Lett. **46**, 7207 (2019).
[31] D. Huyghebaert, G. Hussey, J. Vierinen, K. McWilliams, and J.-P. St-Maurice, ICEBEAR: An all-digital bistatic coded continuous-wave radar for studies of the E region of the ionosphere, Radio Sci. **54**, 349 (2019).
[32] A. Lozinsky, G. Hussey, K. McWilliams, D. Huyghebaert, and D. Galeschuk, ICEBEAR-3D: A low elevation imaging radar using a non-uniform coplanar receiver array for E region observations, Radio Sci. **57**, e2021RS007358 (2022).
[33] D. M. Gillies, J. Liang, E. Donovan, and E. Spanswick, The apparent motion of STEVE and the picket fence phenomena, Geophys. Res. Lett. **47**, e2020GL088980 (2020).
[34] S. G. Shepherd, Altitude-adjusted corrected geomagnetic coordinates: Definition and functional approximations, J. Geophys. Res. **119**, 7501 (2014).
[35] See Supplemental Material http://link.aps.org/supplemental/10.1103/PhysRevLett.134.145201 for additional frequency-dependent correlation akin to Fig. 3, as well as a brief discussion of lower-band chorus waves in the same context, which includes Refs. [36–40].
[36] W. Li, R. M. Thorne, V. Angelopoulos, J. Bortnik, C. M. Cully, B. Ni, O. LeContel, A. Roux, U. Auster, and W. Magnes, Global distribution of whistler-mode chorus waves observed on the THEMIS spacecraft, Geophys. Res. Lett. **36**, L09104 (2009).
[37] M. Spasojevic and U. S. Inan, Drivers of chorus in the outer dayside magnetosphere, J. Geophys. Res. **115**, A00F09 (2010).
[38] H. Aryan, J. Bortnik, D. G. Sibeck, and G. Hospodarsky, Global map of chorus wave sizes in the inner magnetosphere, J. Geophys. Res. **127**, e2021JA029768 (2022).
[39] R. N. Troyer, A. N. Jaynes, D. P. Hartley, N. P. Meredith, M. Hua, and J. Bortnik, Substorm driven chorus waves: Decay timescales and implications for pulsating aurora, J. Geophys. Res. **129**, e2023JA031883 (2024).
[40] K. Hosokawa and Y. Ogawa, Pedersen current carried by electrons in auroral D-region, Geophys. Res. Lett. **37** (2010).
[41] N. C. Maynard, A. Bahnsen, P. Christophersen, A. Egeland, and R. Lundin, An example of anticorrelation of auroral particles and electric fields, J. Geophys. Res. **78**, 3976 (1973).
[42] Y. Miyoshi, I. Shinohara, T. Takashima, K. Asamura, N. Higashio, T. Mitani, S. Kasahara, S. Yokota, Y. Kazama, S.-Y. Wang, S. W. Y. Tam, P. T. P. Ho, Y. Kasahara, Y. Kasaba, S. Yagitani, A. Matsuoka, H. Kojima, Y. Katoh, K. Shiokawa, and K. Seki, Geospace exploration project ERG, Earth Planets Space **70**, 101 (2018).
[43] N. A. Tsyganenko and M. I. Sitnov, Modeling the dynamics of the inner magnetosphere during strong geomagnetic storms, J. Geophys. Res. **110**, 2004JA010798 (2005).
[44] J. E. Borovsky and J. Bonnell, The dc electrical coupling of flow vortices and flow channels in the magnetosphere to the resistive ionosphere, J. Geophys. Res. **106**, 28967 (2001).
[45] Y. Kasahara, Y. Kasaba, H. Kojima, S. Yagitani, K. Ishisaka, A. Kumamoto, F. Tsuchiya, M. Ozaki, S. Matsuda, T. Imachi, Y. Miyoshi, M. Hikishima, Y. Katoh, M. Ota, M. Shoji, A. Matsuoka, and I. Shinohara, The plasma wave experiment (PWE) on board the Arase (ERG) satellite, Earth Planets Space **70**, 86 (2018).
[46] A. Kumamoto, F. Tsuchiya, Y. Kasahara, Y. Kasaba, H. Kojima, S. Yagitani, K. Ishisaka, T. Imachi, M. Ozaki, S. Matsuda, M. Shoji, A. Matsuoka, Y. Katoh, Y. Miyoshi, and T. Obara, High frequency analyzer (HFA) of plasma wave experiment (PWE) onboard the Arase spacecraft, Earth Planets Space **70**, 82 (2018).
[47] S. Kasahara, S. Yokota, T. Mitani, K. Asamura, M. Hirahara, Y. Shibano, and T. Takashima, Medium-energy particle experiments—Electron analyzer (MEP-e) for the exploration of energization and radiation in geospace (ERG) mission, Earth Planets Space **70**, 69 (2018).
[48] Q. Q. Shi, X.-C. Shen, A. M. Tian, A. W. Degeling, Q. Zong, S. Y. Fu, Z. Y. Pu, H. Y. Zhao, H. Zhang, and S. T. Yao, Magnetosphere response to solar wind dynamic pressure change, in *Dayside Magnetosphere Interactions* (American Geophysical Union (AGU), 2020), Chap. 5, pp. 77–97, 10.1002/9781119509592.ch5.
[49] Y. Miyoshi, A. Morioka, H. Misawa, T. Obara, T. Nagai, and Y. Kasahara, Rebuilding process of the outer radiation belt during the 3 November 1993 magnetic storm: NOAA and Exos-D observations, J. Geophys. Res. **108**, SMP3-1 (2003).
[50] N. P. Meredith, R. B. Horne, R. M. Thorne, and R. R. Anderson, Survey of upper band chorus and ECH waves: Implications for the diffuse aurora, J. Geophys. Res. **114**, A07218 (2009).
[51] B. Ni, R. M. Thorne, N. P. Meredith, R. B. Horne, and Y. Y. Shprits, Resonant scattering of plasma sheet electrons

leading to diffuse auroral precipitation: 2. Evaluation for whistler mode chorus waves, J. Geophys. Res. **116**, A03208 (2011).

[52] B. H. Ahn, H. W. Kroehl, Y. Kamide, D. J. Gorney, S. I. Akasofu, and J. R. Kan, The auroral energy deposition over the polar ionosphere during substorms, Planet. Space Sci. **37**, 239 (1989).

[53] S. Matsuda, Y. Kasahara, H. Kojima, Y. Kasaba, S. Yagitani, M. Ozaki, T. Imachi, K. Ishisaka, A. Kumamoto, F. Tsuchiya, M. Ota, S. Kurita, Y. Miyoshi, M. Hikishima, A. Matsuoka, and I. Shinohara, Onboard software of plasma wave experiment aboard Arase: Instrument management and signal processing of waveform capture/onboard frequency analyzer, Earth Planets Space **70**, 75 (2018).

[54] A. Matsuoka, M. Teramoto, R. Nomura, M. Nosé, A. Fujimoto, Y. Tanaka, M. Shinohara, T. Nagatsuma, K. Shiokawa, Y. Obana, Y. Miyoshi, M. Mita, T. Takashima, and I. Shinohara, The ARASE (ERG) magnetic field investigation, Earth Planets Space **70**, 43 (2018).

[55] Y. Miyoshi, Y. Katoh, T. Nishiyama, T. Sakanoi, K. Asamura, and M. Hirahara, Time of flight analysis of pulsating aurora electrons, considering wave-particle interactions with propagating whistler mode waves, J. Geophys. Res. **115** (2010).

[56] M. Fukizawa, T. Sakanoi, Y. Miyoshi, K. Hosokawa, K. Shiokawa, Y. Katoh, Y. Kazama, A. Kumamoto, F. Tsuchiya, Y. Miyashita, Y. M. Tanaka, Y. Kasahara, M. Ozaki, A. Matsuoka, S. Matsuda, M. Hikishima, S. Oyama, Y. Ogawa, S. Kurita, and R. Fujii, Electrostatic electron cyclotron harmonic waves as a candidate to cause pulsating auroras, Geophys. Res. Lett. **45**, 12,661(2018).

[57] X. Fang, C. E. Randall, D. Lummerzheim, W. Wang, G. Lu, S. C. Solomon, and R. A. Frahm, Parameterization of monoenergetic electron impact ionization, Geophys. Res. Lett. **37**, L22106 (2010).

[58] J. M. Picone, A. E. Hedin, D. P. Drob, and A. C. Aikin, NRLMSISE-00 empirical model of the atmosphere: Statistical comparisons and scientific issues, J. Geophys. Res. **107**, SIA 15-1 (2002).

[59] M. Fukizawa, T. Sakanoi, Y. Miyoshi, Y. Kazama, Y. Katoh, Y. Kasahara, S. Matsuda, A. Kumamoto, F. Tsuchiya, A. Matsuoka, S. Kurita, S. Nakamura, M. Shoji, M. Teramoto, S. Imajo, I. Shinohara, S.-Y. Wang, S. W.-Y. Tam, T.-F. Chang, B.-J. Wang, and C.-W. Jun, Statistical study of approaching strong diffusion of low-energy electrons by chorus and ECH waves based on *in situ* observations, J. Geophys. Res. **127**, e2022JA030269 (2022).

[60] H. J. Opgenoorth, I. Hägström, P. J. S. Williams, and G. O. L. Jones, Regions of strongly enhanced perpendicular electric fields adjacent to auroral arcs, J. Atmos. Terr. Phys. **52**, 449 (1990).

[61] B. S. Lanchester, K. Kaila, and I. W. McCrea, Relationship between large horizontal electric fields and auroral arc elements, J. Geophys. Res. **101**, 5075 (1996).

[62] R. A. Greenwald, Diffuse radar aurora and the gradient drift instability, J. Geophys. Res. (1896–1977) **79**, 4807 (1974).

[63] M. J. Schmidt and S. P. Gary, Density gradients and the Farley-Buneman instability, J. Geophys. Res. (1896–1977) **78**, 8261 (1973).

[64] M. Oppenheim, N. Otani, and C. Ronchi, Saturation of the Farley-Buneman instability via nonlinear electron $E \times B$ drifts, J. Geophys. Res. **101**, 17273 (1996).

[65] N. F. Otani and M. Oppenheim, A saturation mechanism for the Farley-Buneman instability, Geophys. Res. Lett. **25**, 1833 (1998).

[66] J. P. St-Maurice, W. Kofman, and E. Kluzek, Electron heating by plasma waves in the high latitude E-region and related effects: Observations, Adv. Space Res. **10**, 225 (1990).

[67] J.-P. St-Maurice and L. Goodwin, Revisiting the behavior of the E-region electron temperature during strong electric field events at high latitudes, J. Geophys. Res. **126**, A11322 (2021).

[68] K. Hosokawa, A. Kadokura, N. Sato, S. E. Milan, M. Lester, G. Bjornsson, and Th. Saemundsson, Electric field modulation behind pulsating aurora, J. Geophys. Res. **113** (2008).

[69] M. F. Ivarsen, Y. Jin, A. Spicher, W. Miloch, and L. B. N. Clausen, The lifetimes of plasma structures at high latitudes, J. Geophys. Res. **126**, e2020JA028117 (2021).

[70] M. F. Ivarsen, J.-P. St-Maurice, J. Park, J. Klenzing, Y. Jin, and W. Lee, Plasma structure decay rates in the equatorial ionosphere are strongly coupled by turbulence, Geophys. Res. Lett. **51**, e2024GL109441 (2024).

[71] Y. Miyoshi *et al.*, The ERG science center, Earth Planets and Space **70**, 96 (2018).

[72] S. Kasahara *et al.*, The MEP-e instrument level-3 flux data of Exploration of energization and Radiation in Geospace (ERG) Arase satellite, Version v01.01. ERG Science Center, Institute for Space-Earth Environmental Research, Nagoya University (2018), 10.34515/DATA.ERG-02003.

[73] Y. Kasahara *et al.*, The PWE/OFA instrument Level-2 power spectrum data of Exploration of energization and Radiation in Geospace (ERG) Arase satellite, 10.34515/DATA.ERG-08000.

[74] Y. Kasahara *et al.*, The PWE/HFA instrument Level-2 spectrum data of Exploration of energization and Radiation in Geospace (ERG) Arase satellite (2018), 10.34515/DATA.ERG-10000.

[75] A. Matsuoka *et al.*, The MGF instrument level-2 spin-fit magnetic field data of Exploration of energization and Radiation in Geospace (ERG) Arase satellite, Version v03.04. ERG Science Center, Institute for Space-Earth Environmental Research, Nagoya University (2018), 10.34515/DATA.ERG-06001.

[76] G. Hussey and M. Ivarsen, ICEBEAR 3D coherent scatter radar data for 2020, Version 2 (2021), 10.5281/zenodo.7509022.

[77] P. T. Newell and J. W. Gjerloev, Evaluation of SuperMAG auroral electrojet indices as indicators of substorms and auroral power, J. Geophys. Res. **116**, A12211 (2011)..

[78] N. E. Papitashvili and J. H. King, OMNI 1-min Data (2020), https://omniweb.gsfc.nasa.gov/.

[79] TREx RGB, UCalgary Space Remote Sensing Group Data Landing Page—UCalgary SRS Data documentation (2023), 10.11575/4P8E-1K65.

[80] R. T. Tsunoda, High-latitude F region irregularities: A review and synthesis, Rev. Geophys. **26**, 719 (1988).

[81] M. Ivarsen, D. Huyghebaert, Y. Jin, Y. Miyashita, J.-P. St.-Maurice, G. Hussey, B. Dan, S. Kasahara, K. Song, P. Jayachandran, S. Yokota, Y. Miyoshi, Y.

Kasahara, I. Shinohara, and A. Matsuoka, Transient, turbulent Hall currents in the sunlit terrestrial ionosphere, Research Square Pre-print Repository (2025), 10.21203/rs.3.rs-5313766/v2
[82] M. F. Ivarsen, J.-P. St-Maurice, G. C. Hussey, D. Galeschuk, A. Lozinsky, B. Pitzel, and K. A. McWilliams, An algorithm to separate ionospheric turbulence radar echoes from those of meteor trails in large data sets, J. Geophys. Res. **128**, e2022JA031050 (2023).
[83] T. N. Davis and M. Sugiura, Auroral electrojet activity index AE and its universal time variations, J. Geophys. Res. **71**, 785 (1966).
[84] W. Baumjohann and R. Nakamura, 5.03—Magnetospheric contributions to the terrestrial magnetic field, in *Treatise on Geophysics*, 2nd ed. edited by G. Schubert (Elsevier, Oxford, 2007), pp. 79–90, 10.1016/B978-0-444-53802-4.00097-X.
[85] J. F. Vickrey, R. R. Vondrak, and S. J. Matthews, The diurnal and latitudinal variation of auroral zone ionospheric conductivity, J. Geophys. Res. **86**, 65 (1981).
[86] V. Coumans, J.-C. Gérard, B. Hubert, M. Meurant, and S. B. Mende, Global auroral conductance distribution due to electron and proton precipitation from IMAGE-FUV observations, Ann. Geophys. **22**, 1595 (2004).
[87] P. T. Newell, T. Sotirelis, and S. Wing, Diffuse, monoenergetic, and broadband aurora: The global precipitation budget, J. Geophys. Res. **114**, A09207 (2009).
[88] E. Bland, F. Tesema, and N. Partamies, D-region impact area of energetic electron precipitation during pulsating aurora, Ann. Geophys. **39**, 135 (2021).
[89] J. D. Sahr and B. G. Fejer, Auroral electrojet plasma irregularity theory and experiment: A critical review of present understanding and future directions, J. Geophys. Res. **101**, 26893 (1996).
[90] M. M. Oppenheim, Y. Dimant, and L. P. Dyrud, Large-scale simulations of 2-D fully kinetic Farley-Buneman turbulence, Ann. Geophys. **26**, 543 (2008).
[91] B. G. Fejer and M. C. Kelley, Ionospheric irregularities, Rev. Geophys. **18**, 401 (1980).

End Matter

Appendix A: A graphic representation of the findings—Figure 5(a) illustrates the electrodynamics of the conjugate measurements analyzed in the present Letter. Intense electric fields, which point in the direction of moving ions, are organized in some pattern outside of pulsating auroral patches [23]. The field points away from downward (likely thermal) currents and toward the upward currents (auroras). Surrounding the pulsating patches are plasma density gradients [22].

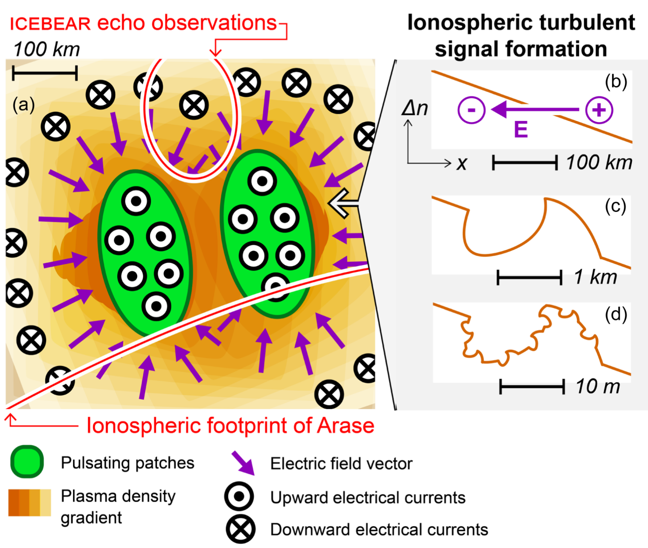

FIG. 5. (a) Annotated schematic depiction of the electrodynamics surrounding the ICEBEAR and *Arase* measurements. (b) A schematic representation of a density structure near one of the pulsating patches in (a), along the density gradient (Δn), and with an applied electric field ($\boldsymbol{E}$). Together these may generate sub-kilometer-scale turbulent structures through the gradient-drift instability. The irregular structures can further decay into smaller-and-smaller pieces, until they may seed the meter-scale Farley-Buneman instability, itself likewise triggered by $\boldsymbol{E}$. (b)–(d) 100× magnifications of the foregoing panel.

Figures 5(b)–5(d) illustrate how this description can turn into turbulent energy dissipation, as the density structures in Fig. 5(a) become gradient-drift unstable [62,80]. The resulting waves decay into smaller-and-smaller turbulent branches, until they may act as seeds for the meter-scale Farley-Buneman instability. Thus, a turbulent signal is formed by "the ensemble" of 3-m Farley-Buneman waves, one whose temporal characteristics approach that of the wave power, the underlying driver.

The approximate measurement locations of those two matching turbulent signals are indicated around the pulsating patches in the electrodynamic diagram in Fig. 5(a), and Figs. 5(b) and 5(c) illustrate the turbulent signal formation in the lower ionosphere.

Appendix B: Part of a trend?—We argue that the clear-cut event analyzed in the present Letter is part of a trend, where Ref. [81] presents relevant evidence for this trend from the day-side polar ionosphere. Indeed, the turbulent Hall channels that may frequent the vicinity of diffuse auroras, in general, are highly localized in time and space, like most research into the "spiky" nature of electric field enhancements can attest to [60]. To support such a general connection between magnetospheric wave-particle energy and subsequent modulations to the ICEBEAR echo detection rates, we have fallen back on inferences made from statistics.

We aggregated the echo detection rates between magnetic local times of 20 and 06 h, a distribution that is

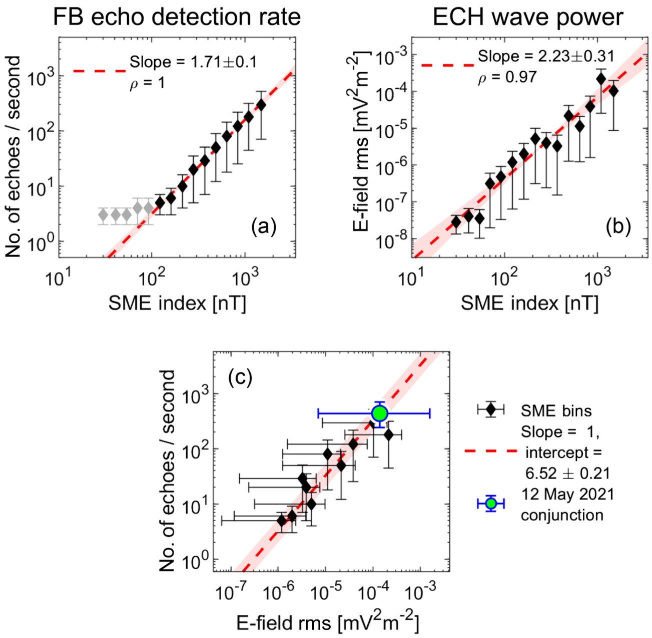

FIG. 6. The ICEBEAR echo detection rate, (a) for some 1.2×10^6 1-s intervals (containing a total of 272×10^6 echoes) and (b) the *Arase*-observed wave rms ($f > 2f_e$) for some 530 000 1-s wave spectra. Black diamonds represent the median value of 15 logarithmically spaced SME index bins, and vertical error bars denote upper (lower) quartile distributions. Linear fits are indicated, by nonlinear least squares minimization of the root-mean-square error, and error margins are posted showing 95% confidence intervals of the fits (3σ). (c) Shows the same bins in a scatter plot, with a red dashed line denoting a 1:1 relation. The data were collected between January 2020 and June 2023 during days when the radar was operational. Data from the May 12, 2021 event are shown with a green circle.

roughly consistent with surveys of ECH waves [50,51]. We took the raw number of echoes per second after removing bins with a mean signal-to-noise ratio lower than 1.5, which removes the occasional radio interference, and discarding bins in which only a single echo was detected. We subsequently aggregated *Arase* ECH wave power rms for frequencies $f > 2f_e$, when the satellite was within 5° of the equator at the same magnetic local time interval, and with a Northern Hemisphere orbital footprint between 60° and 72° MLAT.

In Figs. 6(a) and 6(b), we show the resulting median values for the echo detection rates and wave power, respectively, in 15 geomagnetic activity bins. In Fig. 6(a), we observe a distinct kink in the curve at an SME-index value of around 150 nT, below which the echo detection rate is flat (indicating a contamination by meteor trail echoes [82]). For bins above this kink, the bin-median echo detection rate is perfectly correlated ($\rho = 1$) with the SME index. The linear slope (1.71 ± 0.11 in a log-log scale) is roughly consistent with the slope exhibited by the wave power data [Fig. 6(b)], 2.23 ± 0.31.

The two quantities exhibit a similar response to enhancements in the SME index. This facilitates the 1:1 relationship shown in Fig. 6(c), where we display the same geomagnetic activity bins in a scatter plot [excluding the gray data points in Fig. 6(a) as well as the equivalent bins in Fig. 6(b)], and a log-log linear fit with slope 1 is shown with a red, dashed line. Finally, with a green-blue circle, we show the median values derived from the May 12, 2021 event, with error bars denoting upper (lower) quartile distributions.

Figures 6(a) and 6(b) show two widely different geophysical quantities—one in the ionosphere and one in the magnetosphere—that nevertheless respond in a similar fashion to a *third* independent variable, the SME index. Indeed, that index is itself an unambiguous measurement from the ground of the ionosphere's high-latitude Hall currents (the auroral electrojets) [83,84]. Enhancements in Hall conductance are, in turn, driven by energetic particle precipitation [85,86], by virtue of providing ionization and causing electric field enhancements. As we detail in the present Letter (and illustrate in Fig. 5), the same two quantities are able to drive Farley-Buneman turbulence.

In empirical terms, the diffuse and pulsating auroras constitute the majority of the total energy input into the night-side ionosphere [87], and so enhancements in the Hall currents there are largely driven by diffuse and pulsating auroras [22,88].

The ICEBEAR echo rate reflects the amplitude and spatial extent of any large-amplitude meter-scale Farley-Buneman-generated turbulence in the electrojets within the radar field of view [89–91].

The above chain of argument explains why $\rho = 1$ in Fig. 6(a): Global though it may be, and thus not expected to correlate with the echo rates during individual events, the SME index encapsulates the average response of the ICEBEAR data in the face of an externally driven magnetosphere.